Fan, Qitang; Yan, Linghao; Trip, Matthias R.; Krejci, Ondrej; Dimosthenous, Stavrina; Kachel, Stefan R.; Chen, Mengyi; Foster, Adam; Liljeroth, Peter; Gottfried, J. Michael

Biphenylene network: A nonbenzenoid carbon allotrope

Published in:
Science

DOI:
10.1126/science.abg4509

Published: 21/05/2021

Document Version
Peer-reviewed accepted author manuscript, also known as Final accepted manuscript or Post-print

Please cite the original version:
Fan, Q., Yan, L., Trip, M. R., Krejci, O., Dimosthenous, S., Kachel, S. R., Chen, M., Foster, A., Liljeroth, P., & Gottfried, J. M. (2021). Biphenylene network: A nonbenzenoid carbon allotrope. *Science*, *372*(6544), 852-856. https://doi.org/10.1126/science.abg4509

Biphenylene Network: A Nonbenzenoid Carbon Allotrope

Qitang Fan[1,4], Linghao Yan[2,4], Matthias W. Tripp[1], Ondřej Krejčí[2], Stavrina Dimosthenous[2], Stefan R. Kachel[1], Mengyi Chen[1], Adam S. Foster[2,3], Ulrich Koert[1], Peter Liljeroth[2]*, J. Michael Gottfried[1]*

[1]Department of Chemistry, Philipps-Universität Marburg, Hans-Meerwein-Straße 4, 35032 Marburg, Germany

[2]Department of Applied Physics, Aalto University, FI-00076 Aalto, Finland

[3]Nano Life Science Institute (WPI-NanoLSI), Kanazawa University, Kakuma-machi, 920-1192 Kanazawa, Japan

[4]These authors contributed equally to this work

*Corresponding authors. Email: peter.liljeroth@aalto.fi (P.L.); michael.gottfried@chemie.uni-marburg.de (J.M.G.)

Abstract:

The quest for planar sp^2-hybridized carbon allotropes other than graphene, such as graphenylene and biphenylene network, has stimulated substantial research efforts because of the materials' predicted mechanical, electronic, and transport properties. However, their syntheses remain challenging given the lack of reliable protocols for generating non-hexagonal rings during the in-plane tiling of carbon atoms. Here, we report the bottom-up growth of ultraflat biphenylene network with periodically arranged four-, six-, and eight-membered rings of sp^2-hybridized carbon atoms, through on-surface inter-polymer dehydrofluorination (HF-zipping) reaction. The characterization of this biphenylene network by scanning probe methods reveals that it is metallic rather than a dielectric. We expect the interpolymer HF-zipping method to complement the toolbox for the synthesis of other nonbenzenoid carbon allotropes.

One Sentence Summary:

A planar carbon network with four-, six- and eight-membered rings is obtained via an on-surface synthesis approach.

Main Text:

The synthesis of fullerenes (*1*), carbon nanotubes (*2*), graphene (*3*), and cyclo[18]carbon (*4*) from customized molecular precursors has initiated the era of designer carbon allotropes built from sp, sp^2, and sp^3-hybridized carbon atoms (*5*). Although numerous sp^2-hybridized planar carbon allotropes such as graphene (*6*), pentaheptite (*7*), and biphenylene network (*8*) were proposed (Fig. 1**A**), only graphene has been realized as a purely hexagonal net (*3*). Progress in the synthesis of other planar 3-coordinate carbon nets (*6*) with non-hexagons such as 4-, 5-, 7-, 8-membered rings has been very limited. Recently, expanding on the highly successful bottom-up synthesis of benzenoid graphene-related nanostructures (*9-13*), several nonbenzenoid nanographenes (*14-17*) and nanoribbons (*18-20*) with embedded nonhexagonal rings were reported.

Nevertheless, these carbon nanostructures only exhibit repeating nonhexagonal motifs along one dimension, which has hampered the study of the properties of planar nonbenzenoid carbon allotropes. For instance, the successful synthesis and characterization of a biphenylene polymer chains cannot serve to clarify the theoretical debate on whether biphenylene network is dielectric (*21*) or metallic (*22, 23*). Attempts to add nonhexagonal carbon rings along the second dimension through hierarchical polymerization of nonbenzenoid molecules were of limited success. For example, the lateral fusion of polyazulene chains yielded only small segments of phagraphene (*24*), a planar carbon net with 5-, 6-, and 7-membered rings, because the orientation of the azulene moieties could not be controlled (*25*). Similarly, efforts toward the synthesis of biphenylene network (BPN, Fig. 1**B**) through sequential deiodinative and debrominative coupling of 1,4,5,8-tetraiodo-2,3,6,7-tetrabromobiphenylene (TTBP, Fig. 1**B**) failed at the initial polymerization step (*26*).

Here, we demonstrate an alternative approach, in which the nonbenzenoid structural elements were not contained in the precursor, but formed during the lateral dehydrofluorination (HF-zipping) fusion of benzenoid polyphenylene chains. As shown in Fig. 1**C**, 4,4’’-dibromo-2,2’,2’’,5,5’,5’’-hexafluoro-1,1’:4’,1’’-terphenyl (DHTP) first polymerized through debrominative coupling (*27*) on a Au(111) surface and formed well-aligned assemblies of poly(2,5-difluoro-para-phenylene) (PFPP) chains. In a second step, these chains underwent C-C coupling by HF-zipping (*28-31*) to form a biphenylene network. The interchain HF-zipping allowed C-C bond formation exclusively between a C-F and a C-H moiety (as marked by cyan ovals in Fig. 1**C**), but not between two C-H or two C-F moieties. As a result, 4- and 8-membered rings formed selectively between the chains. Adequately positioned C-F moieties were essential for the formation of the nonbenzenoid structure. In their absence, such as in the case of plain poly(para-phenylene) chains, dehydrogenative C-C coupling led to the formation of 6-membered rings and thus to regular graphene (*32, 33*).

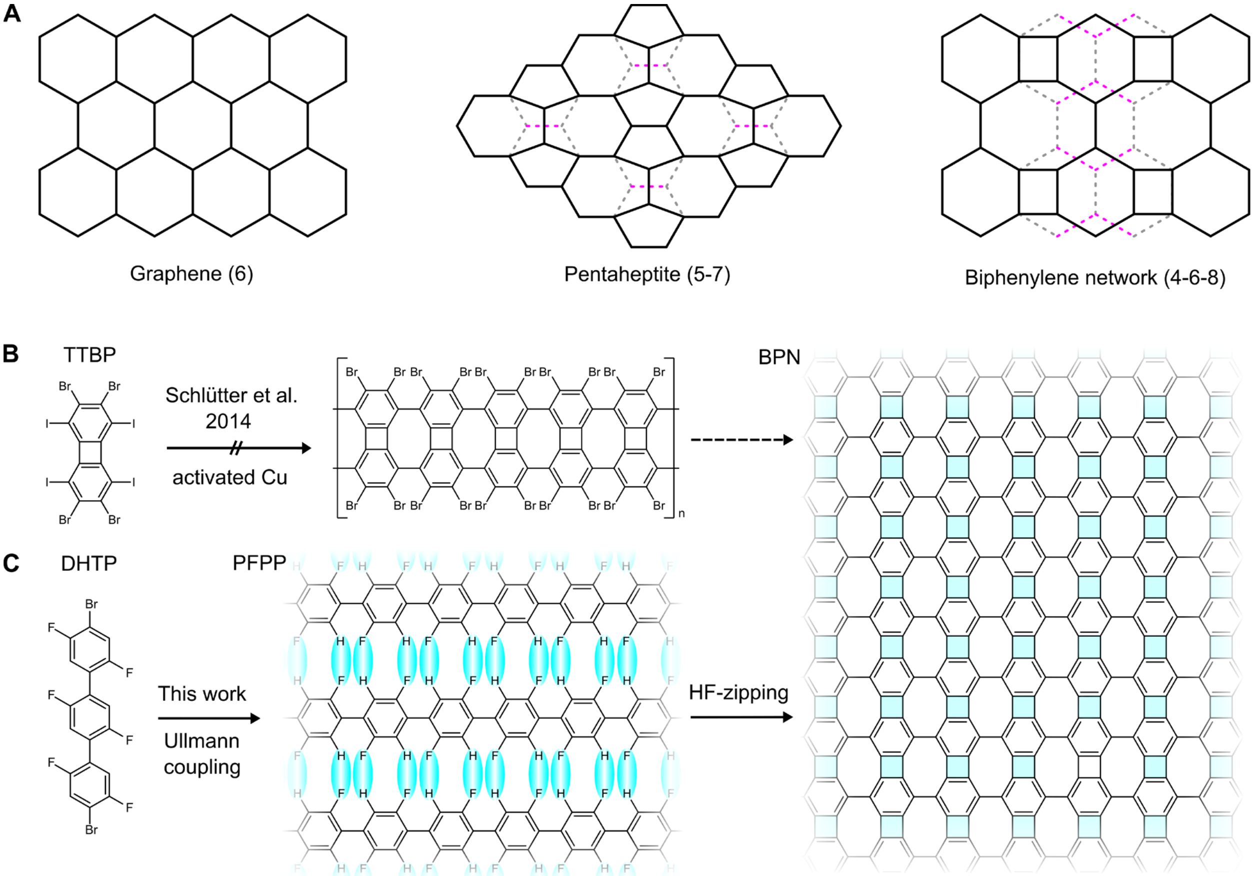

Fig. 1. Synthetic strategies towards the planar nonbenzenoid biphenylene network (BPN). (**A**) Lattice structures of three planar carbon allotropes: graphene, carbon pentaheptite (5-7), and biphenylene network (4-6-8). The latter two formally result from graphene by reorganization of bonds (magenta dotted lines). (**B**) Previous attempts towards the synthesis of BPN from the TTBP monomer. (**C**) DHTP monomer forming BPN by a two-step sequence consisting of linear polymerization followed by inter-chain HF-zipping.

The monomer DHTP was synthesized in solution through a two-step sequence, as described in supplementary materials (materials and methods), and then vapor-deposited in ultrahigh vacuum onto a clean Au(111) surface held at 300 K. Related scanning tunneling microscopy (STM) images are shown in Fig. S1. Subsequent annealing to 500 K induced the formation of PFPP chains by debrominative C-C coupling. An ordered island of well-aligned PFPP chains (Fig. 2**A**) exhibited a pronounced zigzag appearance in the zoom-in STM image in Fig. 2**D**. The periodicity of 8.8 ± 0.2 Å along the chain arose from alternating up-down tilting of the 2,5-difluoro-para-phenylene (FPP) units, as illustrated by the overlaid chemical structure on Fig. 2**D**. This model was confirmed by the non-contact atomic force microscopy (nc-AFM) image in Fig. S2**B**.

The aligned PFPP chains fused laterally through HF-zipping to form a biphenylene network during annealing to 680 K, as shown by the STM image in Fig. 2**B**. This condensation reaction resulted in considerable lateral contraction. The high-resolution nc-AFM images (Fig. 2, **E** and **F**) of the regions marked by the white rectangles in Fig. 2**B** revealed armchair-edged biphenylene ribbons (BPR) with a width of 12 and 18 carbon atoms (12-BPR and 18-BPR). These BPRs have alternating H/F edge-termination, rather than pure H termination, as illustrated by the chemical structure in Fig. 2**E** and confirmed by the simulated AFM images in Figs. S3,4. The widest ribbon (21-BPR) we observed was achieved by further annealing the sample in Fig. 2**B** to 700 K (Fig. 2**C**).

The selectivity for biphenylene network formation is related to the 2D chirality of the PFPP chains. Only HF-zipping between chains of identical handedness led to 4- and 8-membered rings (4-8 type fusion, labeled in Fig. 2**D**). Otherwise, 6-membered rings formed (6-6 type fusion, see Fig. 2**D**), resulting in the formation of an armchair-edged graphene nanoribbon (6-AGNR) with the normal benzenoid topology (Fig. S6). The 4-8 type fusion was overall favored ((2.4 ± 0.3):1 over the 6-6 type, see supplementary text and Fig. S8 for the yield analysis), because each PFPP domain consisted mainly of chains with identical handedness, e.g., the R_a handedness in Fig. 2**D** (see also Fig. S5). Therefore, the aggregation of the PFPP chains in almost homochiral domains was essential for the formation of biphenylene network. Furthermore, sufficient length of the PFPP chains is a prerequisite for the formation of wide BPRs, as is discussed in supplementary text.

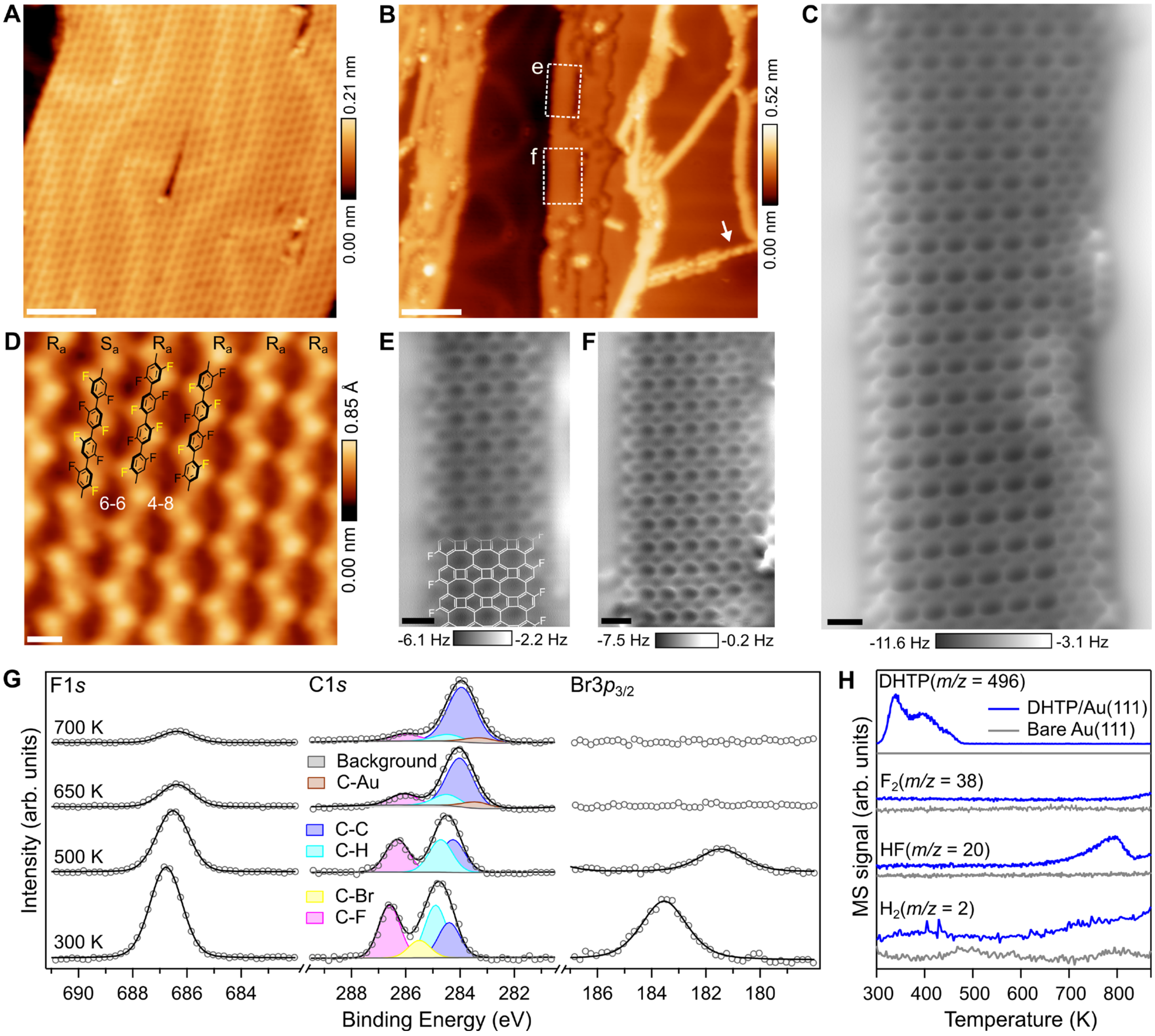

Fig. 2. Formation of biphenylene network by two-step polymerization of DHTP. (**A**,**B**) Overview STM images taken after deposition of DHTP onto Au(111) at 300 K followed by post-annealing to 500 K (**A**) and 680 K (**B**). The white arrow in panel (**B**) marks a remaining PFPP chain for comparison. (**C**) nc-AFM image of a wide biphenylene ribbon (BPR) obtained by further annealing of the sample in panel (**B**) to 700 K. Note that the BPR is jointed with regular graphene at the right side due to minor parasitic 6-6 type fusion. (**D**) Zoom-in STM image of the PFPP chains in panel (**A**) overlaid with chemical structures; 2D enantiomers labeled with R_a and S_a. (**E**,**F**) Zoom-in nc-AFM images of the BPRs outlined by the white rectangles in panel (**B**). Panel (**E**) is overlaid with the chemical structure. Scale bars: (**A** and **B**) 5 nm; (**C** to **F**) 0.5 nm. (**G**) XPS spectra for the indicated core levels and

annealing temperatures. (**H**) Mass spectrometer signals for the indicated *m*/*z* values recorded during controlled heating (1 K/s) of bare and monolayer DHTP-covered Au(111).

The reaction progress was monitored by x-ray photoelectron spectroscopy (XPS) (Fig. 2**G**) and temperature-programmed desorption (TPD) mass spectrometry (Fig. 2**H**). For as-deposited DHTP on Au(111) at 300 K (Fig. 2**G**, 300 K), the F1*s* (686.8 eV) and Br3$p_{3/2}$ (183.5 eV) binding energies were typical for C-F and C-Br groups (*28, 34*) and confirmed that carbon-halogen bonds were intact. The C1*s* signal could be consistently deconvoluted into four components attributed to C-F (pink), C-Br (yellow), C-H (cyan) and C-C (blue) with 1:3:3:2 intensity ratios, in agreement with the composition of DHTP. XPS also confirmed the formation of PFPP chains at 500 K: Lowering of the Br3$p_{3/2}$ binding energy by 2.1 eV indicates C-Br bond dissociation (*34*), and the C1*s* signal could be deconvoluted into three components (1:1:1) representing C-F, C-H, and C-C bonds (Fig. 2**G**, 500 K), in agreement with the chemical structure of the chains. The slight overall shifts (-0.3 eV) of C1*s* and F1*s* signals we attributed to a work-function change (*35*), whereas their attenuation (35% less) was caused by partial desorption of DHTP, as confirmed by the TPD signal of DHTP in Fig. 2**H**.

The gradual attenuation of the F1*s* and C-F related C1*s* signals upon further annealing (Fig. 2**G**, 650 K and 700 K) was indicative of partial removal of fluorine from the C-F groups by HF-zipping. The corresponding TPD trace confirmed HF release above 600 K (Fig. 2**H** and Fig. S9). Note that the C1*s* spectra at 650 K and 700 K showed a component at 283.4 eV, labelled C-Au, which we attributed to benzyne intermediates bonding to the surface after removal of H/F pairs in PFPP chains (Fig. S11). This component decreased from 650 to 700 K because of the progressive fusion of the PFPP chains. Therefore, we tentatively propose the coexistence of HF-zipping (major reaction pathway) and the benzyne-based mechanism (minor reaction pathway) for the lateral fusion of PFPP chains (see supplementary text and Fig. S10).

We systematically characterized BPRs of different widths with scanning tunneling spectroscopy (STS) and DFT calculations. Figure 3**A** shows the normalized differential conductance (d*I*/d*V*) spectra of six different BPRs with widths from 6 to 21 carbon atoms. The spectra were taken at the positions marked by the colored dots in the AFM images on the left sides of Figs. 3, **B** to **G**. The narrower BPRs (6-BPR to 12-BPR) showed distinct valence band (VB) and conduction band (CB) onsets (see also additional d*I*/d*V* spectra and maps in Figs. S13 and S14). Detecting the resonances in the d*I*/d*V* spectra corresponding to the band onsets in the wider BPRs (15-BPR to 21-BPR) was more difficult because of the narrow gaps and extra features around zero bias potentially arising from the Au(111) surface state.

We used d*I*/d*V* maps (Figs. 3, **B** to **G**, middle and right panels, Exp. column) to identity which features in the d*I*/d*V* spectra corresponded to states with similar symmetry compared to the VB and CB of the narrower BPRs (see also additional d*I*/d*V* spectra and maps in Fig. S15-17). These features matched the simulated d*I*/d*V* maps of the VB and CB onsets (Figs. 3, **B** to **G**, middle and right panels, Theory column). For 21-BPR, we could detect orbital features in the d*I*/d*V* maps (Fig. 3**G** and Fig. S17**B**) at all bias voltages, indicating the closing of the gap corresponding to metallic electronic structure. In addition, based on comparison with simulation, the zero bias d*I*/d*V* map corresponded to a mixture of the VB and CB features (arising from states at different momenta, see Fig. S19 for calculated band structures), again consistent with the metallic response.

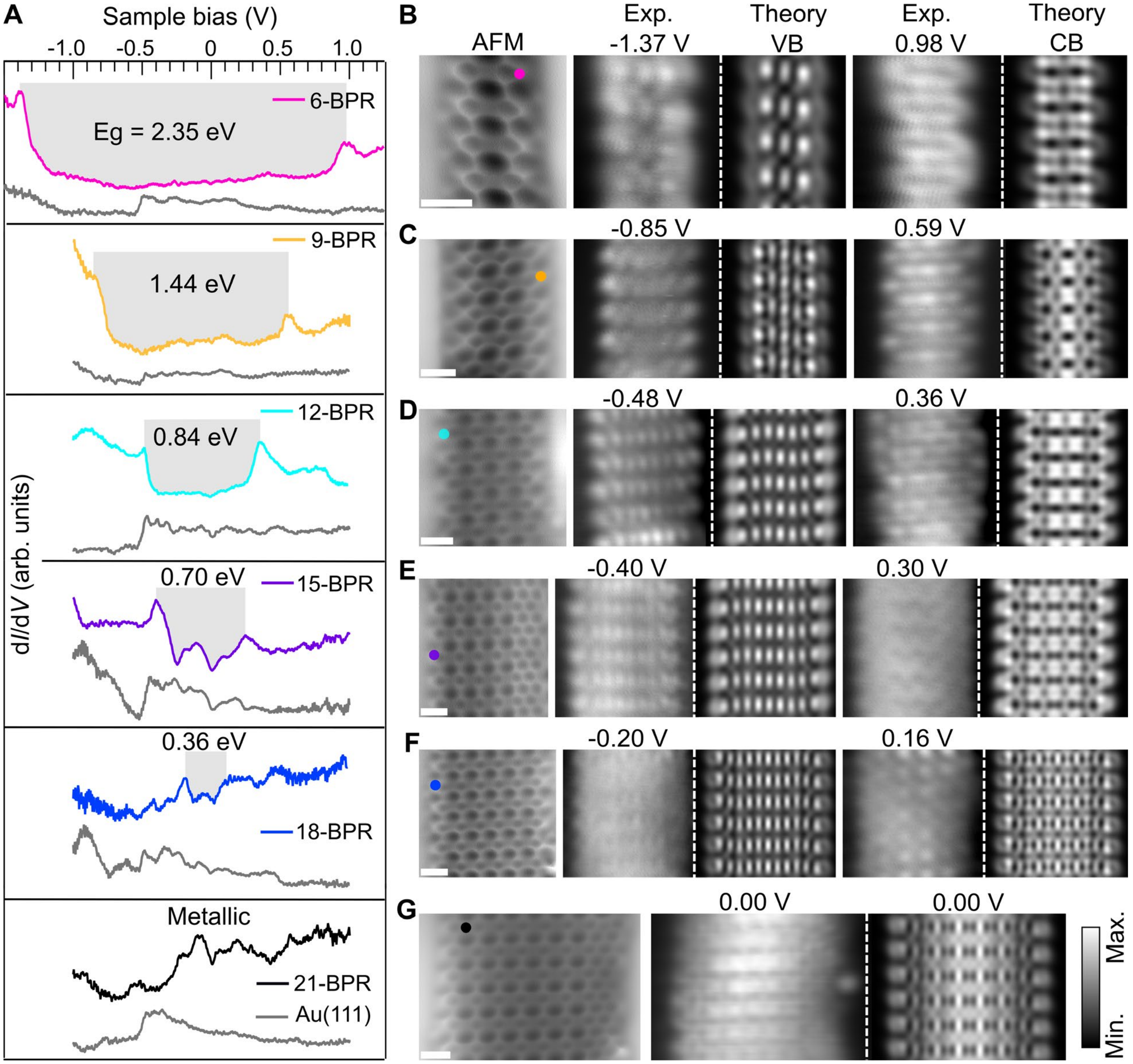

Fig. 3. Electronic properties of BPRs with different widths. (**A**) Differential conductance (d*I*/d*V*) spectra (colored curves) taken at the positions marked with corresponding colored dots in the left parts of panels (**B**-**G**). The gray curves are reference d*I*/d*V* spectra taken at clean Au(111). The shaded regions denote the bandgaps between the peaks related to VB and CB onsets. (**B**-**G**) nc-AFM images, experimental and simulated d*I*/d*V* maps at the VB and CB onsets of the 6-BPR (**B**), 9-BPR (**C**), 12-BPR (**D**), 15-BPR (**E**), 18-BPR (**F**), and 21-BPR (**G**). These nc-AFM images are cut-outs of the nc-AFM images in Figs. 2**C**,**E**,**F** and Figs. S12**C**-**E**. The simulated d*I*/d*V* maps are consistent with fluorine substituents at the edges (see Fig. S18 for a detailed comparison), in

agreement with the AFM images. All scale bars: 0.5 nm. The gray scale for all d*I*/d*V* maps is displayed in the right part of the panel (**G**). All d*I*/d*V* spectra and maps were recorded with CO-functionalized tips.

The bandgap evolution of the BPRs with different widths is summarized in Fig. 4. The measured gaps are overall somewhat larger than the values predicted by DFT at the HSE06 level, but the trend of decreasing bandgaps with increasing widths of the BPRs (Fig. 4, magenta line) agreed well with calculations (black line). This decrease was much steeper than that for the corresponding AGNR series reported previously (Fig. 4, blue line) (*33, 36*). In contrast to the benzenoid AGNRs, the bandgap of the nonbenzenoid BPRs closed completely between 18-BPR and 21-BPR. According to the DFT calculations, the edge termination has no substantial influence on the bandgaps of the BPRs (Fig. S19). This result was also consistent with the predicted bandgaps of pure H-terminated BPRs in previous work (*22*) as illustrated by Fig. S20. The rapid decrease of the measured gaps (from 2.35 to 0 eV) of biphenylene networks with increasing sizes provided strong evidence that this material had metallic character, rather than being dielectric with a gap of 2 eV, as was reported in a previous theoretical study (*21*).

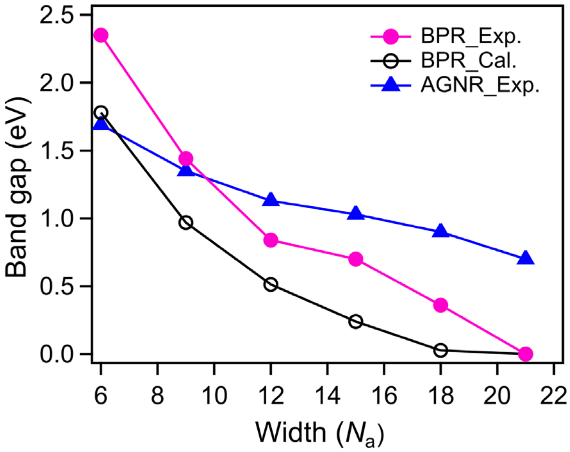

Fig. 4. Comparison between experimental (BPR_Exp., magenta line) and calculated (BPR_Cal., black line) bandgaps of BPRs with AGNRs (AGNR_Exp., blue line) of the same width, as given by the number of carbon atoms, N_a. The AGNR values are adapted from ref. [33] on Au(111) and ref. [36] on AuSIL/Au(111).

Our interpolymer HF-zipping technique for the formation of rings with nonbenzenoid topology in a periodic arrangement paves the way for the exploration of new planar sp^2 carbon allotropes and their properties. Further synthesis progress will focus on increasing yield and selectivity, where the on-surface approach can offer distinct advantages over solution-based reactions (*37*). The HF-zipping reaction is also expected to work on metal-oxide surfaces (*28, 30*), offering decoupling from the metallic substrate. Further direct potential for applications arises from transfer to other substrates or media. For instance, nonbenzenoid 2D carbon allotropes with large rings (> 6) may represent superior anode materials in lithium-ion batteries because of their predicted larger lithium storage capacity compared to graphene (*38*). The revealed metallicity of biphenylene network also makes it a candidate for conducting wires in future carbon-based circuitry.

References and Notes

1. H. W. Kroto, J. R. Heath, S. C. O'Brien, R. F. Curl, R. E. Smalley, C60: Buckminsterfullerene. *Nature* **318**, 162-163 (1985).
2. S. Iijima, T. Ichihashi, Single-shell carbon nanotubes of 1-nm diameter. *Nature* **363**, 603-605 (1993).
3. K. S. Novoselov *et al.*, Electric field effect in atomically thin carbon films. *Science* **306**, 666 (2004).
4. K. Kaiser *et al.*, An sp-hybridized molecular carbon allotrope, cyclo[18]carbon. *Science* **365**, 1299 (2019).
5. A. Hirsch, The era of carbon allotropes. *Nat. Mater.* **9**, 868-871 (2010).
6. A. T. Balaban, Carbon and its nets. *Comput. Math. Appl.* **17**, 397-416 (1989).
7. V. H. Crespi, L. X. Benedict, M. L. Cohen, S. G. Louie, Prediction of a pure-carbon planar covalent metal. *Phys. Rev. B* **53**, R13303-R13305 (1996).
8. A. T. Balaban, C. C. Rentia, E. Ciupitu, Chemical graphs. 6. Estimation of relative stability of several planar and tridimensional lattices for elementary carbon. *Rev. Roum. Chim.* **13**, 231-247 (1968).

9. J. Cai *et al.*, Atomically precise bottom-up fabrication of graphene nanoribbons. *Nature* **466**, 470-473 (2010).

10. D. J. Rizzo *et al.*, Topological band engineering of graphene nanoribbons. *Nature* **560**, 204-208 (2018).

11. P. Ruffieux *et al.*, On-surface synthesis of graphene nanoribbons with zigzag edge topology. *Nature* **531**, 489-492 (2016).

12. L. Yan, P. Liljeroth, Engineered electronic states in atomically precise artificial lattices and graphene nanoribbons. *Adv. Phys. X* **4**, 1651672 (2019).

13. Z. Chen, A. Narita, K. Müllen, Graphene nanoribbons: on-surface synthesis and integration into electronic devices. *Adv. Mater.* 2001893 (2020).

14. S. Mishra *et al.*, On-surface synthesis of a nitrogen-embedded buckybowl with inverse Stone–Thrower–Wales topology. *Nat. Commun.* **9**, 1714 (2018).

15. J. Liu *et al.*, Open-shell nonbenzenoid nanographenes containing two pairs of pentagonal and heptagonal rings. *J. Am. Chem. Soc.* **141**, 12011-12020 (2019).

16. J. Hieulle *et al.*, On-surface route for producing planar nanographenes with azulene moieties. *Nano Lett.* **18**, 418-423 (2018).

17. I. C.-Y. Hou *et al.*, On-surface synthesis of unsaturated carbon nanostructures with regularly fused pentagon–heptagon Pairs. *J. Am. Chem. Soc.* **142**, 10291-10296 (2020).

18. M. Liu *et al.*, Graphene-like nanoribbons periodically embedded with four- and eight-membered rings. *Nat. Commun.* **8**, 14924 (2017).

19. C. Sánchez-Sánchez *et al.*, On-surface synthesis and characterization of acene-based nanoribbons incorporating four-membered rings. *Chem. Eur. J.* **25**, 12074-12082 (2019).

20. J. I. Urgel *et al.*, On-surface synthesis of cumulene-containing polymers via two-step dehalogenative homocoupling of dibromomethylene-functionalized tribenzoazulene. *Angew. Chem. Int. Ed.* **59**, 13281-13287 (2020).

21. N. Tyutyulkov, F. Dietz, K. Müllen, M. Baumgarten, Structure and energy spectra of a two-dimensional dielectric carbon allotrope. *Chem. Phys. Lett.* **272**, 111-114 (1997).

22. M. A. Hudspeth, B. W. Whitman, V. Barone, J. E. Peralta, Electronic properties of the biphenylene sheet and its one-dimensional derivatives. *ACS Nano* **4**, 4565-4570 (2010).

23. N. N. Karaush, G. V. Baryshnikov, B. F. Minaev, DFT characterization of a new possible graphene allotrope. *Chem. Phys. Lett.* **612**, 229-233 (2014).

24. Z. Wang *et al.*, Phagraphene: a low-energy graphene allotrope composed of 5-6-7 carbon rings with distorted dirac cones. *Nano Lett.* **15**, 6182-6186 (2015).

25. Q. Fan *et al.*, Nanoribbons with nonalternant topology from fusion of polyazulene: carbon allotropes beyond graphene. *J. Am. Chem. Soc.* **141**, 17713-17720 (2019).

26. F. Schlütter, T. Nishiuchi, V. Enkelmann, K. Müllen, Octafunctionalized biphenylenes: molecular precursors for isomeric graphene nanostructures. *Angew. Chem. Int. Ed.* **53**, 1538-1542 (2014).

27. W. H. Wang, X. Q. Shi, S. Y. Wang, M. A. Van Hove, N. Lin, Single-molecule resolution of an organometallic intermediate in a surface-supported Ullmann coupling reaction. *J. Am. Chem. Soc.* **133**, 13264-13267 (2011).

28. M. Kolmer *et al.*, Fluorine-programmed nanozipping to tailored nanographenes on rutile TiO_2 surfaces. *Science* **363**, 57-60 (2019).

29. A.-K. Steiner, K. Y. Amsharov, The rolling-up of oligophenylenes to nanographenes by a HF-zipping approach. *Angew. Chem. Int. Ed.* **56**, 14732-14736 (2017).

30. M. Kolmer *et al.*, Rational synthesis of atomically precise graphene nanoribbons directly on metal oxide surfaces. *Science*, **369**, 571-575 (2020).

31. K. Y. Amsharov, P. Merz, Intramolecular aryl–aryl coupling of fluoroarenes through Al_2O_3-mediated HF elimination. *J. Org. Chem.* **77**, 5445-5448 (2012).

32. A. Basagni *et al.*, Molecules–oligomers–nanowires–graphene nanoribbons: a bottom-up stepwise on-surface covalent synthesis preserving long-range order. *J. Am. Chem. Soc.* **137**, 1802-1808 (2015).

33. N. Merino-Diez *et al.*, Width-dependent band gap in armchair graphene nanoribbons reveals fermi level pinning on Au(111). *ACS Nano* **11**, 11661-11668 (2017).

34. D. Han *et al.*, On-surface synthesis of armchair-edged graphene nanoribbons with zigzag topology. *J. Phys. Chem. C* **124**, 5248-5256 (2020).

35. M. Chen *et al.*, Combined photoemission and scanning tunneling microscopy study of the surface-assisted Ullmann coupling reaction. *J. Phys. Chem. C* **118**, 6820-6830 (2014).

36. O. Deniz *et al.*, Revealing the electronic structure of silicon intercalated armchair graphene nanoribbons by scanning tunneling spectroscopy. *Nano Lett.* **17**, 2197-2203 (2017).

37. S. Clair, D. G. de Oteyza, Controlling a chemical coupling reaction on a surface: Tools and strategies for on-surface synthesis. *Chem. Rev.* **119**, 4717-4776 (2019).

38. A. Lherbier *et al.*, Lithiation properties of sp^2 carbon allotropes. *Phys. Rev. Mater.* **2**, 085408 (2018).

39. L. Gross, F. Mohn, N. Moll, P. Liljeroth, G. Meyer, The chemical structure of a molecule resolved by atomic force microscopy. *Science* **325**, 1110-1114 (2009).

40. B. P. Klein *et al.*, Molecular topology and the surface chemical bond: alternant versus nonalternant aromatic systems as functional structural elements. *Phys. Rev. X* **9**, 011030 (2019).

41. V. Blum *et al.*, Ab initio molecular simulations with numeric atom-centered orbitals. *Comput. Phys. Commun.* **180**, 2175-2196 (2009).

42. J. Heyd, G. E. Scuseria, M. Ernzerhof, Hybrid functionals based on a screened Coulomb potential. *J. Chem. Phys.* **118**, 8207-8215 (2003).

43. O. Krejčí, P. Hapala, M. Ondráček, P. Jelínek, Principles and simulations of high-resolution STM imaging with a flexible tip apex. *Phys. Rev. B* **95**, 045407 (2017).

44. P. Hapala, R. Temirov, F. S. Tautz, P. Jelínek, Origin of high-resolution IETS-STM images of organic molecules with functionalized tips. *Phys. Rev. Lett.* **113**, 226101 (2014).

45. P. Hapala *et al.*, Mechanism of high-resolution STM/AFM imaging with functionalized tips. *Phys. Rev. B* **90**, 085421 (2014).

45. W. L. Jorgensen, J. Tirado-Rives, The OPLS [optimized potentials for liquid simulations] potential functions for proteins, energy minimizations for crystals of cyclic peptides and crambin. *J. Am. Chem. Soc.* **110**, 1657-1666 (1988).

47. E. Bitzek, P. Koskinen, F. Gähler, M. Moseler, P. Gumbsch, Structural relaxation made simple. *Phys. Rev. Lett.* **97**, 170201 (2006).

48. B. de la Torre *et al.*, Submolecular resolution by variation of the inelastic electron tunneling spectroscopy amplitude and its relation to the AFM/STM signal. *Phys. Rev. Lett.* **119**, 166001 (2017).

49. B. Maiti *et al.*, Enhancing charge mobilities in selectively fluorinated oligophenyl organic semiconductors: a design approach based on experimental and computational perspectives. *J. Mater. Chem. C* **7**, 3881-3888 (2019).

50. F. Banhart, J. Kotakoski, A. V. Krasheninnikov, Structural defects in graphene. *ACS Nano* **5**, 26-41 (2011).

51. S. Wang *et al.*, Quantum dots in graphene nanoribbons. *Nano Lett.* **17**, 4277-4283 (2017).

Acknowledgements

Funding: Financial support by the Deutsche Forschungsgemeinschaft (DFG) through projects 223848855-SFB1083 and GO1812/2-1, the European Research Council (ERC-2017-AdG no. 788185), and the Academy of Finland (Academy professor funding no.318995 and 320555, and project nos. 311012 and 314882) is gratefully acknowledged. Q.F. thanks the Alexander von Humboldt-Foundation for a Research Fellowship for Postdoctoral Researchers. L.Y. and O.K. acknowledge support from European Union's Horizon 2020 research and innovation program (Marie Skłodowska-Curie Actions Individual Fellowship no. 839242 and no. 845060). A.S.F. has been supported by the World Premier International Research Center Initiative (WPI), MEXT, Japan. This research made use of the Aalto Nanomicroscopy Center (Aalto NMC) facilities. Computing resources from the Aalto Science-IT Project and CSC, Helsinki, are gratefully acknowledged.

Author Contributions: J.M.G., P.L. and U.K. conceived and supervised the experiments. Q.F., L.Y. and M.C. developed the on-surface synthesis protocols and did the STM/AFM measurements and the spectroscopic analysis. M.W.T. synthesized the precursor monomers. S.R.K. did the TPD experiments. O.K. and S.D. performed the simulations under the supervision of A.S.F. Q.F., L.Y., O.K. and S.D. made the figures. Q.F., L.Y., P.L. and J.M.G. co-wrote the paper. All authors discussed the results and commented on the manuscript at all stages; **Competing interests:** The authors declare no competing financial interests. **Data and materials availability:** All data is available in the main text or the supplementary materials.

Supplementary Materials

Materials and Methods

Supplementary Text

Figs. S1 to S24

References (39-51)